PROCEEDINGS, 49th Workshop on Geothermal Reservoir Engineering
Stanford University, Stanford, California, February 12-14, 2024
SGP-TR-227

Newberry Volcano: Reassessing Enigmatic Volcanic-Geothermal System in the Northernmost Basin and Range from Joint Inversion of MT and Gravity Data, and Reappraisal of Legacy Seismic Tomography and Well Data

Adam SCHULTZ[1], Xiaolei TU[1], Alain BONNEVILLE[1], Amanda KOLKER[2], Hannah PAULING[2], and Esteban BOWLES-MARTINEZ[1,3]

[1] Oregon State University, Corvallis OR 97331-5503, USA

[2] National Renewable Energy Laboratory, Golden CO 80401, USA

[3] Pacific Northwest National Laboratory, 902 Battelle Blvd, Richland, WA 99354

Adam.Schultz@oregonstate.edu

Keywords: joint inversion, multiphysics, EGS, hydrothermal, blind play, volcanic, superhot

ABSTRACT

Newberry Volcano, long a target for geothermal exploration as well as an EGS demonstrator site, lies at the intersection of the northernmost Basin and Range Province, the High Lava Plains and the Cascade volcanic backarc in central Oregon. The location of the volcanic edifice and surrounding lava flows and cinder cones is structurally controlled, with the edifice intersecting the Walker Rim fault to the south-southwest, the Sisters Fault to the north-west, and the Brothers Fault to the north-east. Newberry caldera was formed at this intersection of crustal features by an explosive eruption 75,000 ybp followed by numerous rhyolitic and basaltic andesite eruptions. The Big Obsidian Flow (BOF), the most recent eruptive feature (1,300 ybp) lies inside the southern caldera rim.

Pauling et al. (2023) reported at the 2023 Stanford Workshop on Geothermal Reservoir Engineering on a 2022 broadband magnetotelluric (BBMT) and gravity campaign by NREL, Enthalpion Energy LLC and personnel from Oregon State University that acquired 43 BBMT and 233 gravity stations primarily from inside the caldera, the south caldera rim and south flank of the volcano. This was carried out under the support of the DEEPEN (DErisking Exploration for multiple geothermal Plays in magmatic ENvironments) project managed by NREL. A highly conductive feature beneath the south rim and flank of the volcano that shallowed near the BOF had been previously suggested by 3-D inversion of BBMT data acquired in 2012 and 2014, as well as legacy BBMT data, but this feature was poorly constrained because of limited MT data in the south flank area.

We report on a joint 3-D gravity + MT inversion of this expanded 2022 and legacy data set of 237 BBMT and 1514 gravity stations, and joint interpretation with previous seismic models. The highly conductive south rim/flank feature (heretofore referred to as SRFF) was confirmed, it is well resolved, and it is of low relative density and seismically slow. The SRFF extends from near the caldera floor at the BOF, deepening to the south beneath the south flank of the volcano to depths of at more than 4 km relative to the caldera floor, and it is not connected to the sub-caldera magma body. The trace of the SRFF lies immediately east of the Walker Rim fault, within the Basin and Range province, and it is also aligned with a system of Holocene mafic flows, cinder cones and fissure vents. Given its proximity to the Walker Rim fault and the association with faults as fluid migration pathways, the SRFF likely represents the aggregate signature of hydrothermal alteration products, hydrothermal fluids, and at depths greater than the current dataset's resolution limit, potentially partial melt. Legacy well GEO N-1, immediately west of the SRFF shows a transition from purely conductive heat flow in the upper 1000 m, and advective/convective heat flow below presumably related to movement of hydrothermal fluids. The presence of smectite as an alteration product of basaltic ash and ash flow tuff has been associated with the top of the conductive zone 675 m below the GEO N-1 well head.

In addition to the SRFF, a series of low seismic v_p, low relative density, highly conductive N-S aligned finger-like features appear just within the resolution limits of the data sets ~15 km south of the caldera center, roughly parallel to the trace of the Walker Rim fault. These features bear further examination as potential extensions of the geothermal target identified beneath the volcano's south rim and flank. For some decades Newberry volcano has been viewed strictly as an EGS development play restricted to the west flank of the volcano. Our reappraisal of legacy seismic, gravity, MT and well data, coupled with the substantial increase in MT and gravity data coverage in 2022 suggests that rather than a single EGS site, Newberry may represent a series of geothermal target fields, including a potential blind hydrothermal play as well as EGS targets ranging from conventional to superhot. Follow-on efforts to drill as close as possible to the SRFF, subject to restrictions against drilling within the boundary of the National Volcanic Monument, is a logical next step to validate this conceptual model.

1. INTRODUCTION

In 2023 at this workshop, Pauling et al. reported on a June – July, 2022 field campaign to acquire broadband magnetotelluric (MT) and gravity stations at Newberry Volcano in central Oregon, USA (Figure 1). The data set was acquired primarily to improve the spatial resolving power of the subsurface electrical resistivity and density structure as determined by inversion of MT and gravity data, with particular focus on the poorly covered south caldera, south caldera rim and south flank area of the volcano. Previous work at Oregon State University (E. Bowles-Martinez and A. Schultz, 2020) indicated that there was a likely an electrically conductive target that shallowed

near the Big Obsidian Flow and that extended beneath the south rim and flank area to depths that were previously associated with partial melt beneath the caldera. With few MT stations in that region, the feature was poorly resolved.

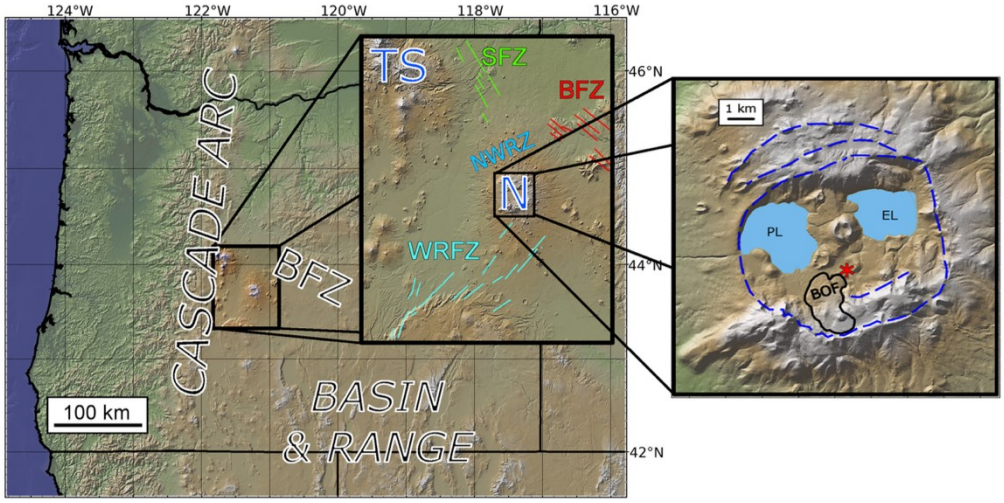

Figure 1. Location of Newberry Volcano at the intersection of major tectonic systems. The inset shows details of the caldera and Newberry's geographic relationship with nearby fault systems and the Three Sisters clusters of volcanoes in the High Cascades. Faults inferred from topography and mapping (MacLeod et al., 1995). BFZ = Brothers Fault Zone; TS = Three Sisters; SFZ = Sisters Fault Zone; WRFZ = Walker Rim Fault Zone; NWRZ = Northwest Rift Zone; N = Newberry; PL = Paulina Lake; EL = East Lake; BOF = Big Obsidian Flow. * marks location of 932-m deep USGS Newberry-2 well (containing hydrothermal fluids). Dashed blue line marks caldera rim and fractures from nested collapse structures, inferred from LIDAR.

The association between the south caldera rim/south flank (SRFF) conductive feature and the seismically determined sub-caldera melt body was not established prior to 2022, given the limitations of the existing data set. By expanding the MT and gravity station coverage in this area the SRFF would be better localized and its significance to evaluation of the geothermal energy potential and volcanic hazards could be better assessed. During the 2022 campaign, 43 BBMT stations were operated on a nominal ~0.5 – 2.5 km spaced grid over an ~86 km^2 area of the caldera and the south caldera rim and south flank of the volcano, with a small area in the northwest flank also instrumented to serve as an MT remote reference site. 233 gravity stations with nominal ~120 – 670 m spacing were completed with seven serving as base stations, with 102 stations at the south flank, 9 on the northwest flank and north caldera rim, and 118 stations at the south caldera rim and south flank of the volcano. The station map is seen in Figure 2.

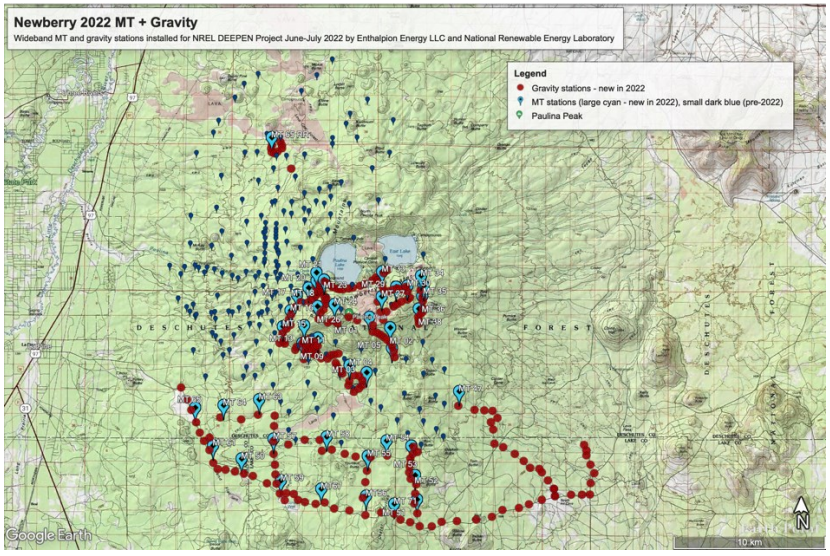

Figure 2. 2022 field program gravity (red markers) and wideband MT array (light blue markers) stations deployed by Enthalpion Energy LLC, personnel from Oregon State University and NREL in June-July 2022 with locations overlaid on topography. Locations of wideband MT stations from legacy data sets included in the analysis and modeling within this project are shown with dark blue markers.

Parts of the 2022 survey were carried out inside the boundaries of Newberry National Volcanic Monument, an area closed to geophysical exploration and geothermal development for several decades. Project contractor Enthalpion Energy LLC worked with the Deschutes

National Forest, Fort Rock District to secure a "Nominal Effects" letter which provided the basis for the survey to proceed without the requirement for a special use permit. This was made possible by employing the subaerial method of MT deployment (Figure 3), a technique developed by Adam Schultz at Oregon State University that arose from discussions with induction coil manufacturer John Saarloos of Geotell, Inc. to enable access to protected sites by eliminating the need to dig holes and trenches to install the MT sensors and equipment. This approach has also been used by the same group at Yellowstone National Park and at Mount Saint Helens National Monument.

Figure 3. (Left) View of Newberry Caldera from NE-to-SW. The Big Obsidian Flow 1300 ybp is the most recent eruptive feature on the volcano. East Lake (on left) and Paulina Lake on right are separated by the Central Pumice Cone. (Right) Three wideband induction coil sensors (white tubes approx. 1-m long) are clamped together and placed on the ground as seen on the left-hand side of the photo. A data acquisition system is located ~5m away (shown here surrounded by crew members on the right-hand side of the photo), powered by a lithium polymer battery pack (green Pelican™-style case) shown in the right foreground. A gravity reading is being taken in the left background of the photo.

2. INVERSION OF GRAVITY AND MAGNETOTELLURIC DATA

We report here on the results of joint inversion of broadband magnetotelluric (MT) and gravity data, along with the joint interpretation of the resulting 3-D electrical resistivity and density models with legacy seismic tomograms. In a later section, we also report on preliminary modeling of the volcanic system using rhyolite-MELTS (Gualda, et al., 2012) to apply constrains from the modeled resistivity, density, and legacy seismic velocity tomograms to constrain the porosity, brine and partial melt content of the sub-caldera magma body and the south caldera rim/south flank (SRFF) anomaly.

Following the individual inversion of the gravity and MT data, joint inversion of these data was carried out to yield final 3-D density and resistivity structure models using a set of inverse modeling codes developed by Dr. Xiaolei Tu. The 3-D MT inversion employs an integral equation forward solver that allows for topography at the surface. The 3-D gravity inversion, also allowing for topography, solves for the variation in density around an average value of 2.5 g/cc.

2a. Augmented Data Set

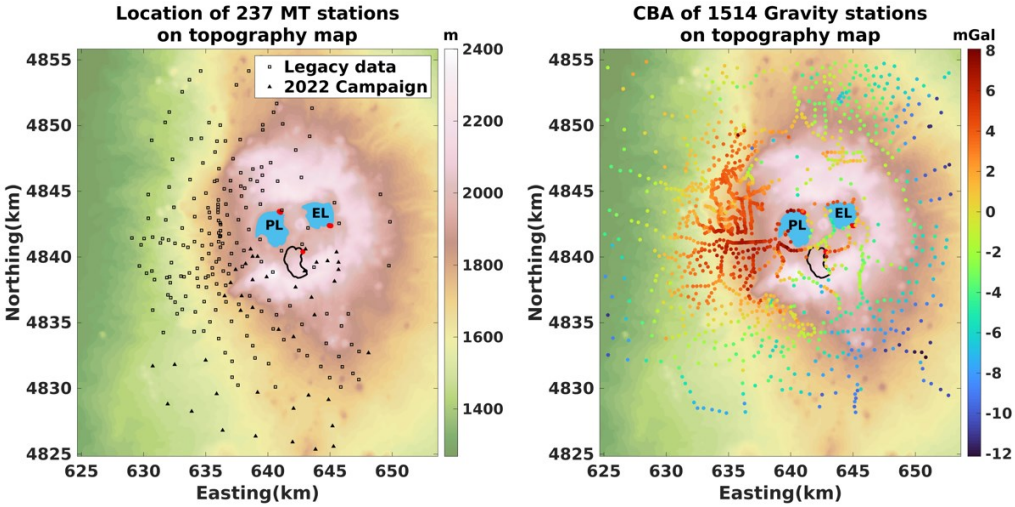

Figure 4. Maps showing the locations of the 237 legacy and new wideband MT stations we operated in 2022 (left) and the Complete Bouguer Anomaly (CBA) data from 1514 legacy and new gravity stations we operated in 2022 (right). PL and EL represent Paulina Lake and East Lake, respectively. The polygonal shape outlined in black immediately SE of PL is the boundary of the Big Obsidian Flow (the most recently erupted feature of Newberry Volcano at 1300 ybp) adjacent to the inside of the south caldera rim. The red dots in the map on the right, above, of the CBA show the locations of hot springs at PL, EL, and near the Big Obsidian Flow.

Prior to inversion for 3-D density structure, the Complete Bouger Anomaly (CBA) and MT data sets were augmented by legacy data available through the Geothermal Data Repository (Figure 4). This includes data released by Davenport Newberry, and by a 2012 and 2014 NETL-Oregon State University-Zonge International project to monitor the EGS Demonstrator Project carried out by AltaRock Energy and partners on the West Flank of Newberry Volcano (Figure 4, see next page).

2b. Formulation of the Inverse Solution

For joint inversion, the following functional was minimized:

$$p(\boldsymbol{m_s}, \alpha, \beta) = \sum_{j=1}^{2} \Phi^{(j)}(\boldsymbol{m_s^{(j)}}) + \sum_{j=1}^{2} \alpha^{(j)} \Psi^{(j)}(\boldsymbol{m_s^{(j)}}) + \beta s\left(\boldsymbol{m_s^{(1)}}, \boldsymbol{m_s^{(2)}}\right) \rightarrow min$$

where $\alpha^{(j)}$ and β are regularization parameters. The misfit and stabilizer functionals are:

$$\Phi^{(j)}\left(m_s^{(j)}\right) = \left\| W_d^{(j)}\left[A^{(j)}\left(m_s^{(j)}\right) - d^{(j)}\right]\right\|_\rho^2,$$

$$\Psi^{(j)}\left(m_s^{(j)}\right) = \left\| W_m^{(j)}(m_s^{(j)} - m_{apr}^{(j)})\right\|^2,$$

where $W_d^{(j)}$ and $W_m^{(j)}$ denote the data and model weights; $d^{(j)}$ is the observed data, i.e., gravity field or MT data. $\| \quad \|_\rho^2$ represents the robust norm. $A^{(j)}$ represents the forward modeling operator for gravity field or MT impedance. The minimization problem is solved with the reweighted regularized conjugate gradient method (RRCG).

The joint inversion approach works to identify structural features that are in common between the density and electrical resistivity distributions in the models. The specific method employed is referred to as Gramian structural coupling.

Implementation of Gramian stabilizer:

$$s\left(\mathbf{m_s^{(1)}}, \mathbf{m_s^{(2)}}\right) = \iiint_D g\left(\nabla \mathbf{m_s^{(1)}}, \nabla \mathbf{m_s^{(2)}}\right) dv,$$

where $g(,)$ is the Gramian of the gradient at the position $\mathbf{r}$; D denotes the inversion domain (Tu & Zhdanov, 2021).

The stabilizer $s\left(\mathbf{m_s^{(1)}}, \mathbf{m_s^{(2)}}\right)$ is minimized if the gradients of the two model parameters are parallel at every point in the inversion domain. Minimizing of s will necessitate the coincidence of structural boundaries of different model parameters.

While there is no requirement, from the perspective of equations of state, for the variations in density and the variations in electrical resistivity to be strictly coincident, experience has shown that coupling the two solutions together through gradient-based approaches helps to stabilize the solutions and to identify real structural boundaries that might otherwise be poorly resolved or missed when inverted using only a single type of data set.

2c. Resolution Analysis

Our resolution matrices are calculated based on the integrated sensitivity, derived from the Jacobian matrix calculated in the inversion, which contains elements $\frac{\partial \|d\|}{\partial m}$, each of which represents the change in the data vector d with respect to a change in a model element value m. This is similar to the derivative weight sum (DWS) routinely used by seismologists but it is more robust. The underlying concept is to measure how sensitive the data as a whole is to the value of physical property (i.e., density or electric resistivity) at each point in the subsurface, which is determined by the data coverage and also by the governing laws of physics.

The power to resolve finer-scale features in the density and resistivity model volumes is calculated from the Jacobian and is displayed in Figure 5 below for a model depth 0.5 km beneath the caldera floor.

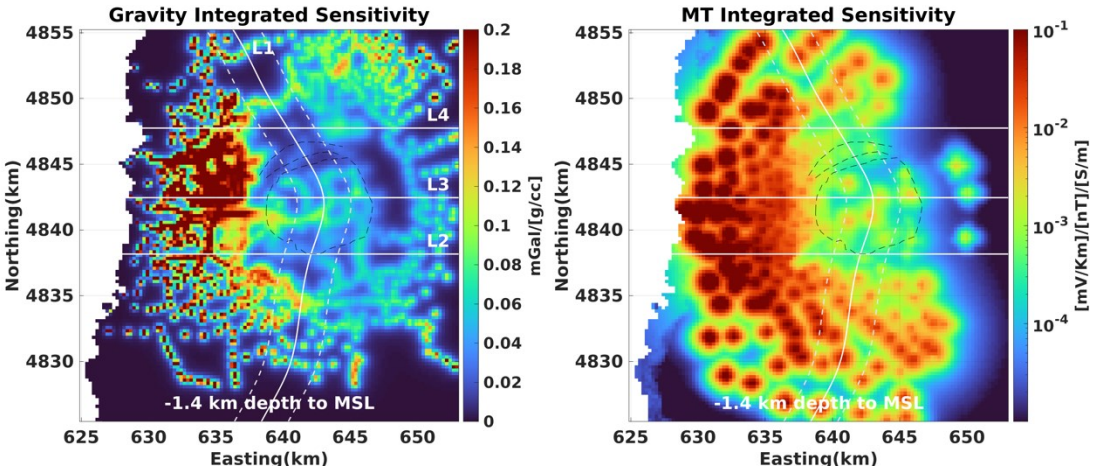

Figure 5. Horizontal sections of integrated sensitivity (resolution) matrices at a depth of 1.4 km above sea level/1 km below Paulina Peak/0.5 km below the caldera floor.

For Figure 5 and all maps that follow, the white lines L1, L2, L3 and L4 are respectively a S-N arcuate section through the center of the caldera tracing the path of the Walker Rim Fault to the south and the Sisters Fault to the north, a W-E section through the south caldera rim, a W-E section through the center of the caldera, and a W-E section through the north caldera rim. Corresponding vertical sections through the 3-D models will be presented following the horizontal sections maps and discussion.

Referring to the gravity integrated sensitivity on the left-hand side of Figure 5, the cool/bluer colors indicate regions where features are more poorly resolved, and the hotter/red colors are where features are best resolved. The units of sensitivity are mGal per g/cc. Dark red colors indicate that a 1 g/cc change in the density of a feature at this depth will result in a 0.25 mGal gravity signal as measured at ground level, while a dark blue region indicates that the same 1 g/cc change in the density of a model feature will produce a much weaker gravity signal with a change that may be near 0 mGal. A 1 g/cc change in the density of a model feature at this depth will therefore be most easily resolved beneath the densely instrumented west flank of the volcano where there are intense warmly colored zones. There is still resolving power along the southwest and southern flanks of the volcano, but it is diminished along the north and northwest rim at these depths. The situation is similar for the resolvability of resistivity features (units mv/km/nT per S/m change in the resistivity of a model feature at this depth), although the areas of best resolvability are broader given the different governing laws for MT to those of gravitation.

At the greater depth of 2.3 km beneath the caldera floor in Figure 6 below, the ability to resolve finer scale features is diminished, but the area over which there is good resolving power is also broadened, to cover the full aperture of the survey arrays.

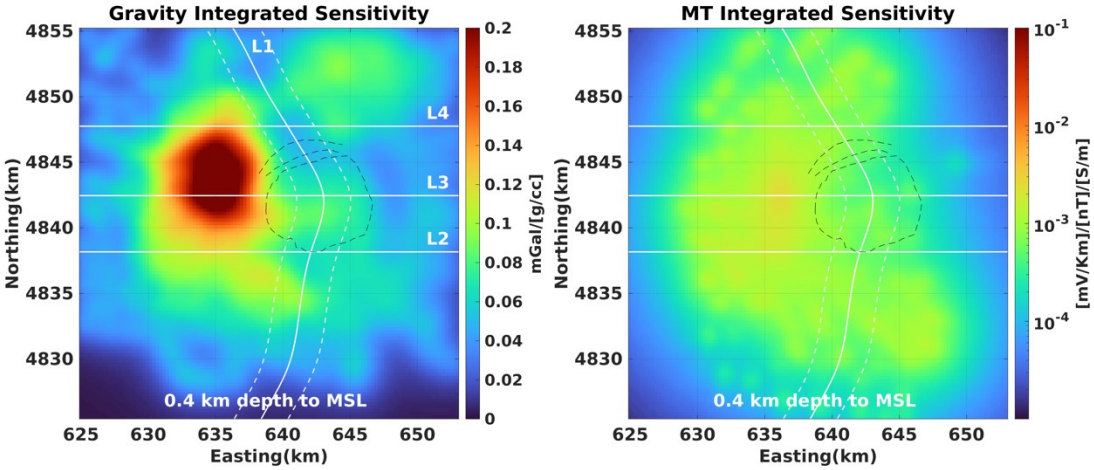

Figure 6. Horizontal sections of integrated sensitivity (resolution) matrices at a depth of 0.4 km above sea level/2.8 km below Paulina Peak/2.3 km below the caldera floor.

2d. 3-D Density and Resistivity Models from Joint Inversion, Horizontal Sections

In the following figures we show a series of map views of density and resistivity at progressively greater depths within the jointly inverted model. Depths of each section are shown with reference to sea level, the top of Paulina Peak, and the caldera floor. For the density model a region of the model is considered adequately resolved if a 1 g/cc change in a model feature at a given depth produces a 0.01 mGal

change in the gravity data. For the resistivity model that threshold is reached when a decade resistivity change (i.e., from 0.1 S/m to 1 S/m) in a model feature at a given depth produces a 0.001 mv/km/nT change in the MT data.

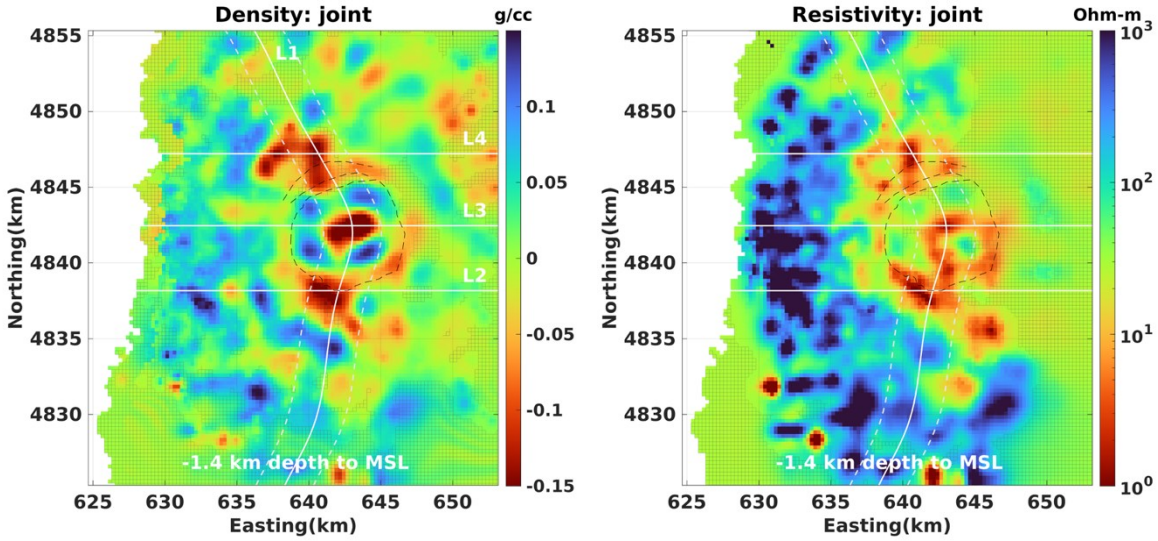

Figure 7. Horizontal sections of jointly inverted models at a depth of 1.4 km above sea level/1.0 km below Paulina Peak/0.5 km below the caldera floor. (left) Density in g/cc relative to an average density of 2.5 g/cc. Denser than average areas are shown in cool colors, less dense than average are shown in warm colors. (right) Electrical resistivity in Ohm-m. More resistive areas are shown in cool colors, more conductive areas in warm colors. The outline of the caldera rim appears as a dashed arcuate line. The stippled gray area denotes parts of the model that are poorly resolved, while all other areas are well resolved, following the resolution analysis in Section 2c above. L1, L2, L3 and L4 are reference lines for vertical model sections shown later.

The irregular white area on the extreme left of each map in Figure 7 identifies parts of the surface of the volcanic edifice with elevations lower than the 1.4 km above MSL reference level for this map section. The grid-shaded areas found mainly on the periphery of each model section are areas of lower resolving power as revealed through analysis of the Jacobian matrix from the joint inversion. Features within the caldera itself, the northwest rim and west flank and the south rim and south flank of the volcano are well resolved in both density and resistivity for this depth section. The density scale from -0.15 to 0.15 g/cc is for density relative to the average of 2.5 g/cc. The electrical resistivity is shown on a $\log_{10}$ color scale, with deep red areas being highly conductive, and deep blue areas highly resistive.

For the depth sections in Figure 7 (0.5 km below the caldera floor) and in Figure 8 (1.0 km below the caldera floor) the primary features are interpreted as surface rubble, brecciated material, caldera infill and surface volcanics. The prominent low relative density and low resistivity feature near the center of the caldera is associated with caldera infill and shallow hydrothermal features. There are hot springs in the two caldera lakes, and temperature wells in the caldera show highly elevated temperatures at these depths near the low resistivity feature near the south caldera rim near the Big Obsidian Flow.

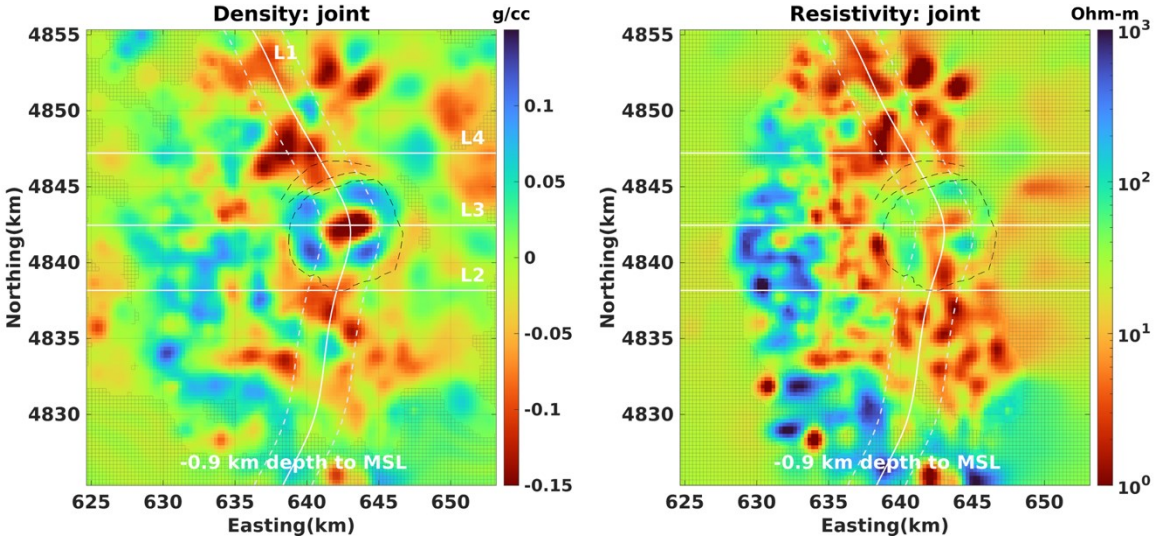

Figure 8. Horizontal sections of jointly inverted models at a depth of 0.9 km above sea level/1.5 km below Paulina Peak/1.0 km below the caldera floor.

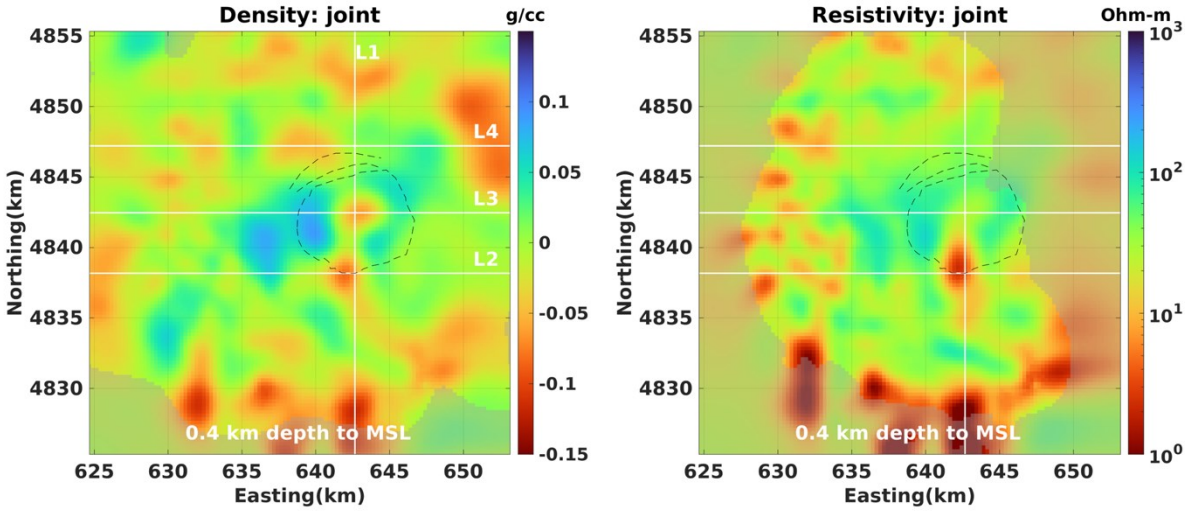

Figure 9. As Figure 8 but horizontal sections of jointly inverted models at a depth of 0.4 km above sea level/2.8 km below Paulina Peak/2.3 km below the caldera floor.

In Figure 9 the density map displays a prominent low-density zone 2.3 km below the caldera floor center. A second prominent low-density zone appears on the south caldera rim and extends to the south-southeast. A series of north-south finger like low density structures appear at the bottom edge of the model section. On the west flank of the volcano, a prominent high-density zone is associated with the enhanced geothermal system development site in that area. This zone is associated with a pluton in a conceptual geological model produced by NETL and Oregon State University (Mark-Moser, et al., 2016). The resistivity map does not show an anomaly in the caldera center, but a strongly conductive feature aligns with the low-density zone in the south caldera rim and flank. This feature is well resolved. The north-south finger like features seen in the density map also appears in the resistivity map, at the bottom edge of the model, although unlike for the density map, the resolving power of these features in the resistivity map is marginal.

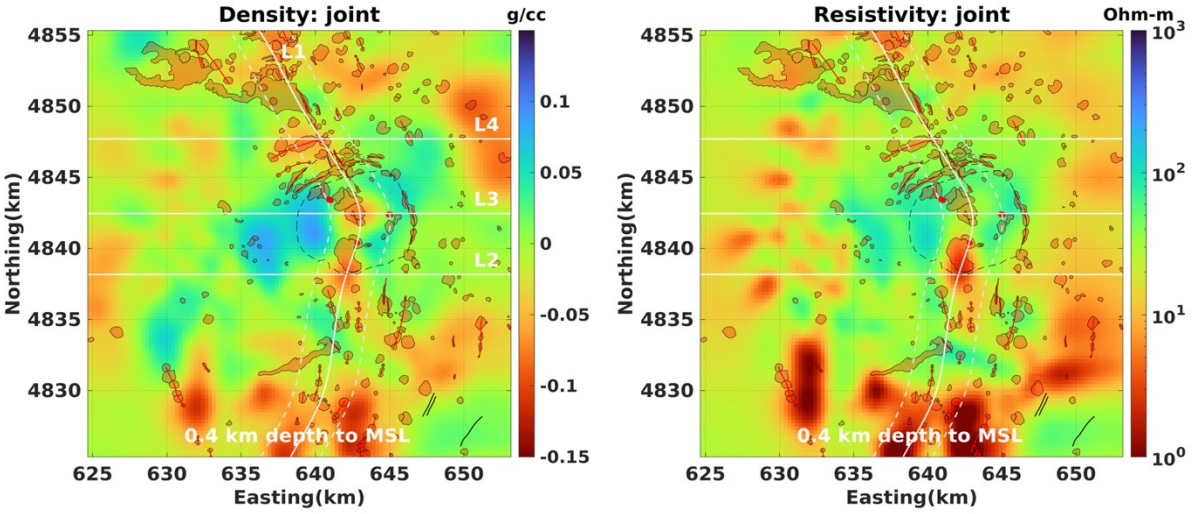

Figure 10. As in Figure 9 but with an overlay of volcanic features in gray (lava flows and cinder cones) and major fault lines in white. The extension into the caldera of the Walker Rim fault to the south-southwest of the caldera and the Sisters fault to the north-northwest is inferred by the authors but it has not been mapped because of the presence of a thick layer of caldera collapse rubble and the presence of the two lakes. Note the association of the surface expression of mapped volcanic features and the SRFF anomaly. Geologic features extracted from MacLeod, et al. (1995).

Figure 10 shows the geographic association between deep fault structures, surface vents, cones and flows and the underlying density and resistivity anomalies 2.3 km below caldera floor depths. Figure 11 illustrates that a seismic tomogram obtained from inversion of data obtained from active seismic shots to the northeast during the NSF-supported High Lava Plains experiment identified a well-localized low velocity zone at ~2 km depth that overlaps the highly conductive, low-density zone imaged through single and joint inversion of the MT and gravity data sets.

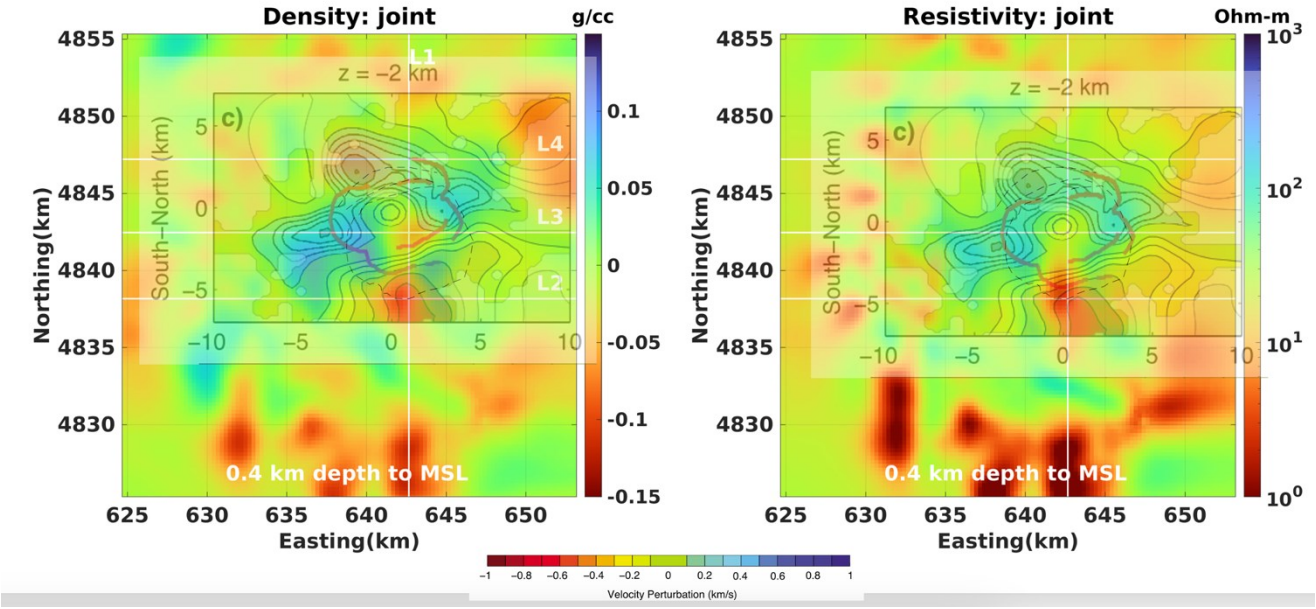

Figure 11. As in Figure 9 but with an overlay of a v_p seismic tomogram from Beachley et al (2012), showing the clear overlap of a pronounced low velocity zone with the SRFF low density, low resistivity zone.

As we extend to greater depths, we note that previous work by Beachley, et al. (2012) suggested that the top of the sub-caldera magma body was likely at depths of 3-4 km below the caldera floor. At similar depths, a conceptual geological model developed by the National Energy Technology Laboratory and Oregon State University from all available geological and geophysical data available prior to 2022 (seismic tomography, seismic waveform analysis, 3-D MT, 3-D gravity, microseismicity, well logs, cores/petrology, heat flow, ground deformation, LIDAR and geologic mapping) produced the image in Figure 12 (Mark-Moser, et al., 2016). The pluton highlighted in that figure on the volcano's west flank corresponds to a density and resistivity anomalies evident in Figure 13 that follows. This west flank region is an area of active EGS R&D. The pluton has been inferred to represent a previous volcanic center.

While not shown in Figure 12, the conceptual geologic model does not contain any feature corresponding to the south rim/south flank (SRFF) anomaly that was (weakly) inferred by 3-D MT modeling carried out prior to collection of the 2022 MT and gravity data set.

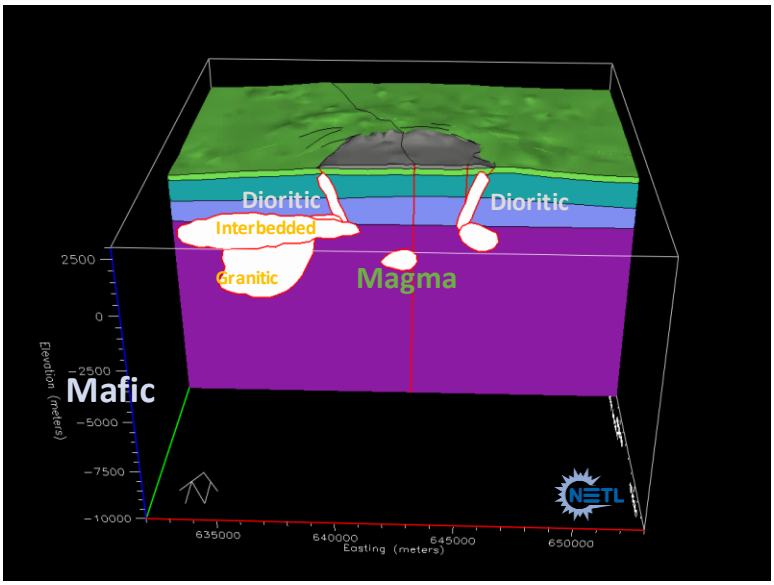

Figure 12. Vertical section through NETL/OSU conceptual geological model of Newberry Volcano. The view is from the south looking northward. Note the presence of a pluton containing interbedded granites underlying surface volcanics beneath the west flank, dioritic ring dikes along the caldera rim, and a small melt body beneath the caldera. Source: Mark-Moser et al, 2016.

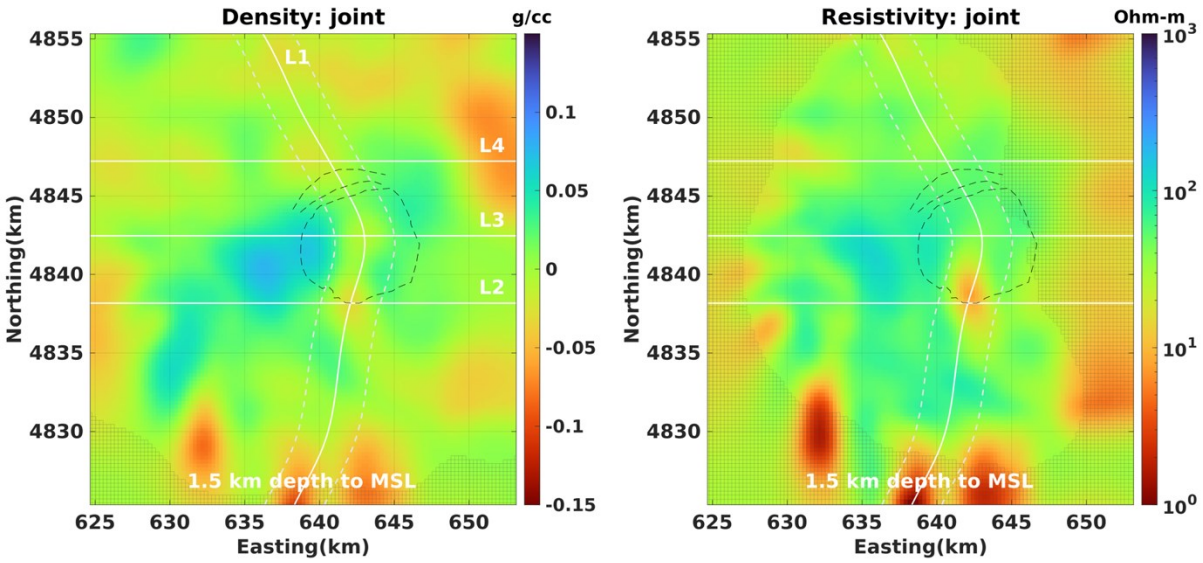

Figure 13. Horizontal sections of joint inverted models at a depth of 1.5 km above sea level/3.9 km below Paulina Peak/3.4 km below the caldera floor.

Four features are most notable in Figure 13, the horizontal model section at a depth of 3.4 km below the caldera floor. First, the denser than average, more resistive zone on the west flank, associated with the impermeable pluton underlying the EGS lease unit is evident from the caldera edge west to an ~ 635 km easting, between 3838 km and 4844 km northing. The low-density zone beneath the caldera center associated with the seismic low velocity feature interpreted by Beachley et al. (2012) as a melt body is barely detectible, and there is essentially no resistivity signature of the feature at these depths. Third, the strong low resistivity and detectible low relative density zone associated with the south caldera rim/south flank (SRFF) anomaly seen previously in Figure 12 persists to these depths. Fourth, the low relative density, low resistivity finger-like features persist along the southern margins of the model. The resolution analysis of the Jacobian matrix indicates that the southern finger-like low density features are well resolved, and they are marginally resolved – primarily at their northernmost extent, as low resistivity zones.

While not shown here, the SRFF continues to greater depth, as do the N-S finger-like structures along the southern edge of model, but the resolving power of the data set decreases significantly at depths below approximately 4.5 km below the caldera floor.

2e. 3-D Density and Resistivity Models from Joint Inversion, Vertical Sections

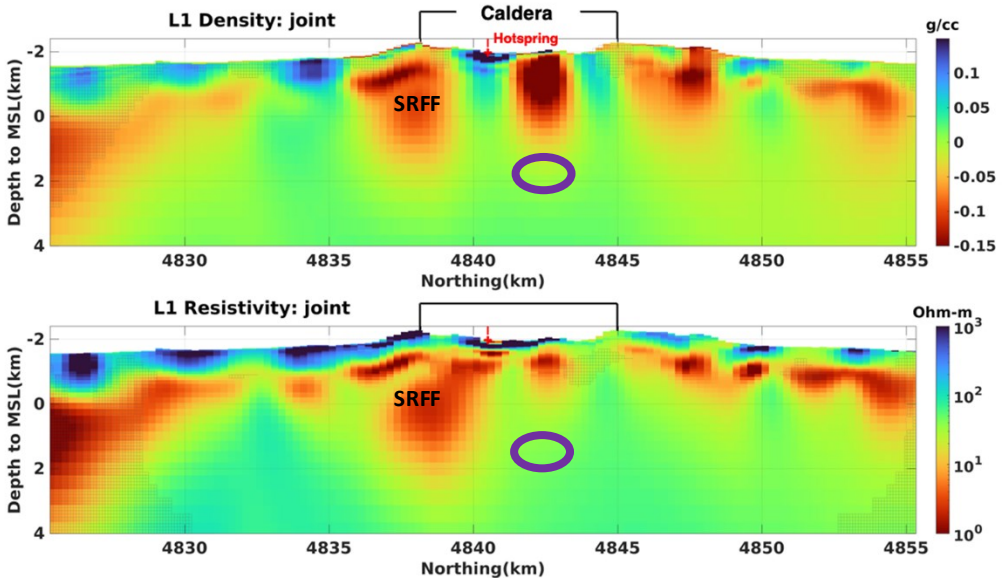

Figure 14. Vertical profiles of jointly inverted models along the L1 arc that runs from south to north through the center of the caldera. Areas of low resolution are shaded with gray stippling. The red cross denotes the location of a hot spring adjacent to the Big Obsidian Flow. The purple outlined ovals represents the approximate depth range of the top of a partial melt body as identified seismically by Beachley et al., 2012. The area marked by SRFF is the western edge of the south rim/south flank feature – the zone of relatively low density and low resistivity.

Figure 14 is a vertical section through the models following a south-to-north line through the center of the caldera. The Central Pumice Cone separating East Lake from Paula Lake in the center of the caldera is located at ~4843 km northing; the south caldera rim at 4837.5 km, and the north caldera rim at 4845 km. Beneath the center of the caldera floor at shallow depth and extending to nearly 1 km MSL there is a prominent low relative density zone that we associate with caldera infill. This is surrounded by an annulus of higher relative density material that is likely associated with dacitic dike structures. A low relative density zone is found on both south and north flanks, although it is most pronounced beneath the south flank where it appears to be connected to a structure that continues to and deepens to the southern edge of the model.

The resistivity section shows a conductive zone at shallow depths beneath the center of the caldera, but extending only to ~-0.5 km MSL, or 1.5 km shallower than the low-density zone. This may be associated with caldera infill and the hydrothermal features seen in and below the caldera lakes. The resistivity section closely matches the density section on the south and north flanks, with a prominent conductive feature under the south rim that appears to shallow inside the caldera near the edge of the Big Obsidian Flow and that deepens to the south where it appears to be connected to the highly conductive, low-density feature that extends to the edge of the model volume. The hachured areas indicating zones of relatively poor resolving power intrude on the southern edge of this feature, but it remains well resolved as far south as 4828 km northing in the resistivity section and 4824 km northing in the density section. Note the absence of a density or resistivity anomaly associated with the sub-caldera seismic low velocity feature identified as a partial melt zone by Beachley et al (2012).

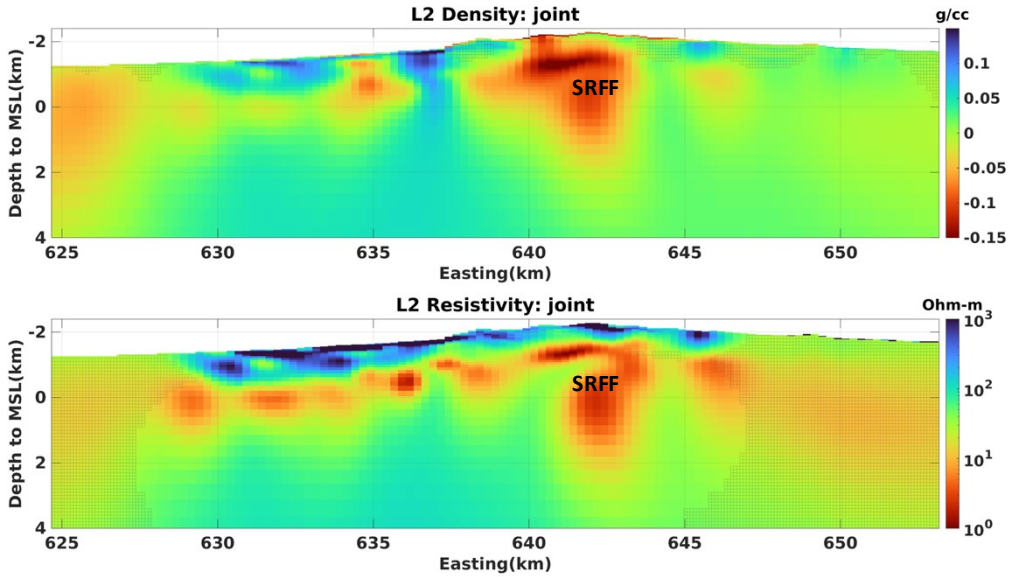

Figure 15. Vertical profiles of jointly inverted models along the L2 line that runs from west to east crossing the south caldera rim. The area marked by SRFF is the core of the south rim/south flank feature – the zone of relatively low density and resistivity.

In the west-to-east vertical section in Figure 15 that crosses the south caldera rim, the highest point along the south caldera rim is at 642 km easting. This is immediately east of the trace of the Walker Rim crustal fault that intersects the volcano from the southwest. The prominent low density, low resistivity feature is found adjacent to and in this area with the deepest part of the feature extending to a depth of 2 km MSL along this profile.

In the section shown in Figure 16, a profile from west-to-east across the center of the caldera, the low-density zone seen in the center of caldera in the horizontal map depth sections is evident, surrounded by higher density dike zones. The low resistivity zone is co-registered with this (at ~ 642-645 km easting) although, as before, it doesn't extend to as great a depth and its horizontal boundaries are not too well resolved. The absence of a density and resistivity anomaly associated with the putative melt body beneath the caldera is noted in this vertical section as well. This is examined further in Figure 17 where we compare the vertical model sections L2 (west-east through the volcano's south caldera rim) and L3 (west-east through the caldera center) on a larger depth scale with the seismic tomography sections of Heath et al. (2015). While Beachley et al. (2012) carried out tomography using active shots along a line from the High Lava Plains to the northeast of Newberry volcano, and they used waveform modeling to constrain the melt body beneath the caldera, Heath et al. (2015) combined active seismic shots data with passive seismic data to produce their tomogram.

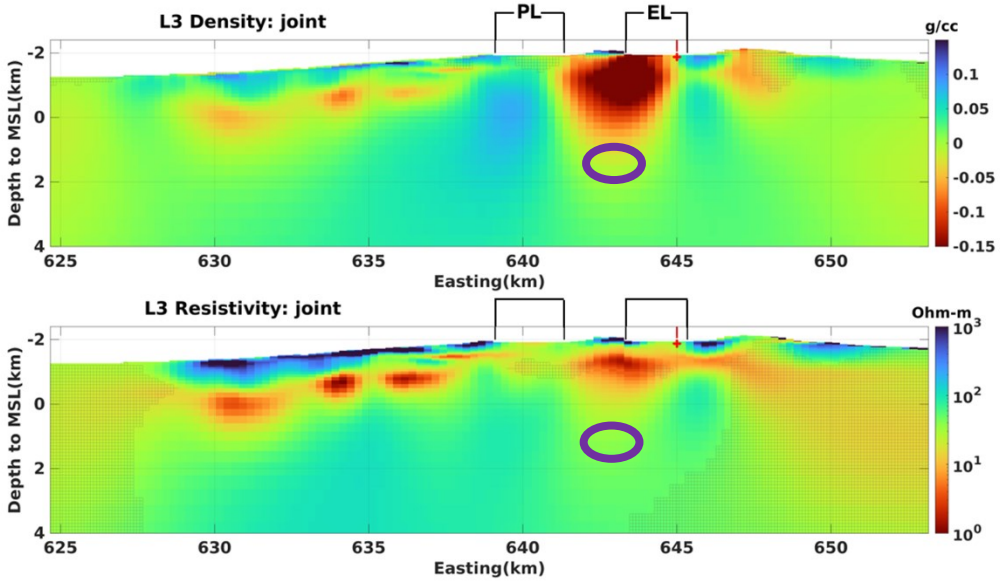

Figure 16. Vertical profiles of jointly inverted models along the L3 line that runs west to east through the caldera center. PL marks the location of Paulina Lake separated by the Central Pumice Cone from EL – East Lake. The purple outlined ovals represents the approximate depth range of the top of a partial melt body as identified seismically by Beachley et al., 2012.

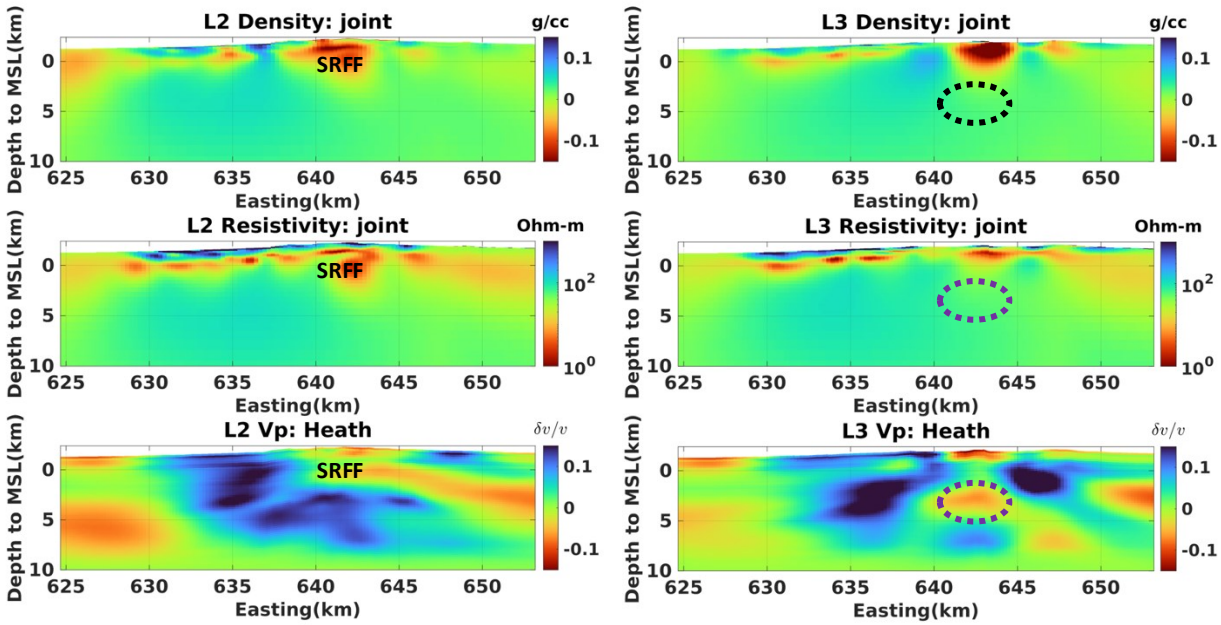

Figure 17. Vertical profiles of jointly inverted models along the L2 Line (left) and L3 line (right) that run from west to east through the south caldera rim and the caldera center, respectively. Note that the depth scale extends to 10 km, and that there is little resolving power in the MT or gravity data set below ~4.5 km.

Figure 17 reveals that the south caldera rim/south flank (SRFF) anomaly has tightly overlapping low density, low resistivity and low v_p velocity zones in the west-to-east vertical section L2 line that crosses the south caldera rim, whereas the low v_p (sub-caldera melt zone) in Heath et al. (2015) does not co-register with a density or resistivity anomaly in the west-to-east vertical section L3 line that crosses the caldera center. Figures 18-20 below provide greater clarity on the geographic relationships between these key observables by displaying on a satellite map view a projection to the surface of isocontours of density, then density overlaid by resistivity and finally density, resistivity and v_p.

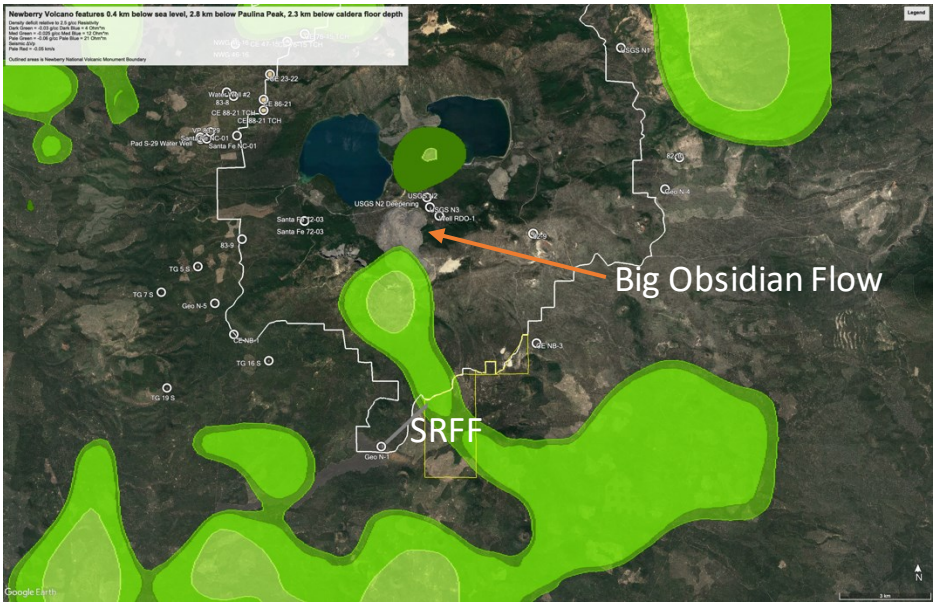

Figure 18. Isocontours of density from the 3-D jointly inverted gravity data model in shades of green, at a depth of 2.3 km below the caldera floor projected onto satellite view of Newberry volcano. Isolines shown are -0.06 g/cc, -0.03 g/cc, -0.025 g cc relative to an average density of 2.5 g/cc. The white polygon is the boundary of Newberry National Volcanic Monument. The yellow outlined polygon that extends southward from the southern boundary of the National Volcanic Monument, and that is crossed by the SRFF is the outline of a geothermal lease owned by the first author of this paper through his company, Enthalpion Energy. Immediately to the west of the SRFF, just at the boundary of the Volcanic National Monument, the GEO N-1 well location is marked. The well and its data are described in more detail in Section 3 of this paper.

In Figure 18, the density signature of the south rim/south flank feature (SRFF) at this depth is seen to extend along the south caldera rim to the southern part of the Big Obsidian Flow and then it continues south-southeast past the caldera rim to the south flank of the volcanic edifice where it joins with the series of N-S low density finger-like structures at the southern edge of the model. The lowest density and lowest resistivity isosurfaces are associated with the south caldera wall edge of the Big Obsidian Flow. Jensen and Chitwood (2000) note that the Big Obsidian Eruptive Sequence, commencing 1,460 ybp was a three-part rhyolite eruption sequence originating from a common vent at the base of the south caldera wall. The association of the vertically extensive nearly plumiform low density, conductive feature in the 3-D joint inverse model with the source of the Big Obsidian Flow is likely more than coincidental.

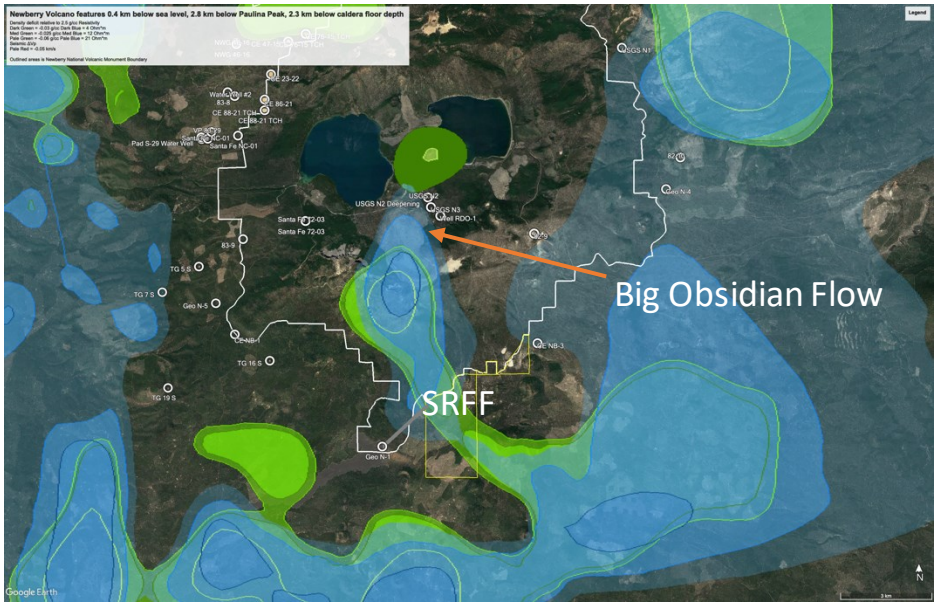

Figure 19. As in Figure 18, but with isocontours of resistivity (in shades of blue) from the 3-D jointly inverted MT data model also superimposed on the previous density isocontours. Resistivity isolines shown are 4 Ωm, 12 Ωm and 21 Ωm, illuminating the most electrically conductive features at a depth of 2.3 km below the caldera floor.

Figure 19 illustrates the geographic overlap of the low density and low resistivity (i.e. highly conductive) zone along the SRFF in the jointly inverted MT and gravity model. While not shown here, individually inverted gravity and MT datasets also show this strong geographic coincidence of density and resistivity anomalies, i.e. this is not an artefact of constraints imposed by the joint inversion.

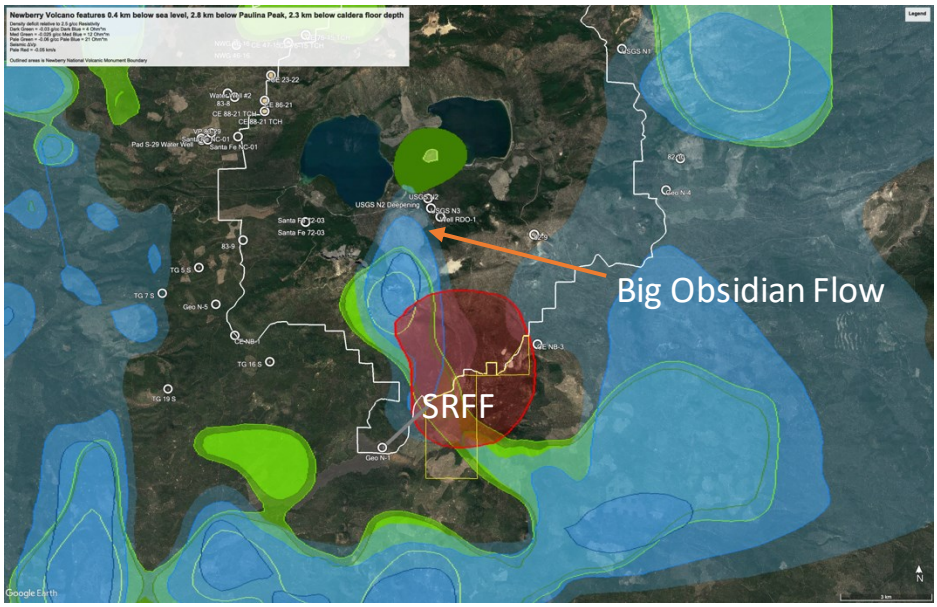

Figure 20. As in Figure 19, but with an isocontour of -0.05 km/s of seismic (v_p) velocity from Heath et al. (2015) in red superimposed on the previous density and resistivity isocontours. At this depth of 2.3 km below the caldera floor, this is the only low velocity anomaly detected within this map area.

Figure 20 makes clear the geographic relationship between the SRFF low density, low resistivity, low v_p features in the jointly inverted MT and gravity data sets, as well as in the Heath et al. (2015) tomogram (which also coincides with a similar low v_p found previously by Beachley et al. (2011)). Beachley et al. considered that the resolving power for the v_p tomogram was poor outside of the caldera, given the use of active seismic shots from the distant northeast of the volcano, and the configuration of seismometers used to receive signals from those shots. Consequently, Beachley et al. placed little confidence was placed on the low velocity zone on the south flank of the volcano. This was less of a concern for the combined active/passive seismic data set and analysis undertaken by Heath et al. (2015). We can conclude with some confidence that the SRFF represents a conductive, low-density, seismically slow feature that geographically shallows under the Big Obsidian flow and that extends and deepens progressively to the south-southeast, eventually joining with N-S finger-like structures on the southern edge of the model.

3. CONSTRAINTS FROM WELL DATA AND FROM MODELING WITH RHYOLITE-MELTS

3.1 Well Data

The GEO N-1 well (seen in Figures 18 – 20) was drilled in 1988 immediately adjacent to the Surveyor Flow within the overall footprint of the Walker Rim Fault Zone on the south flank of the volcano. The weighted mean age for eight geologic sample analyses from the Surveyor Flow is mid-Holocene, at 6,030 +/- 90 ^{14}C yr B.P. (MacLeod et al., 1995). The well is located 2 km southwest of the intersection of the -0.05 km/s low velocity zone with the 12 Ohm-m low resistivity isoline and the -0.03 g/cc low density isoline of the SRFF. Given the proximity of GEO N-1 to the SRFF, downhole conditions are likely to influenced by, and to some degree characteristic of those, within the SRFF.

The most notable features of the downhole temperature profile for GEO N-1 (Figure 21) are the suppressed temperature gradient in the upper ~800 m of the well, the transition from one linear temperature gradient to a somewhat sharper one from 800 m – 1000 m below the well head, and the sharp deviation from linear temperature gradient at depths below that. This is indicative of a transition from purely conductive heat flow in the upper sections with two zones of differing thermal properties, and advective/convective heat flow below presumably related to movement of hydrothermal fluids. The suppressed geothermal gradient above the zone of advective/convective heat flow may be a consequence of heat from below being transported laterally away from the area by the movement of fluids at depth.

The presence of smectite (Figure 21) as an alteration product of basaltic ash and ash flow tuff has been associated with the top of the conductive zone 675 m below the GEO N-1 well head (Fitterman, et al, 1988). At the time this conclusion was drawn, there was little in the way of MT or gravity data for the area around GEO N-1, and the depth extent of the conductive zone was completely unknown.

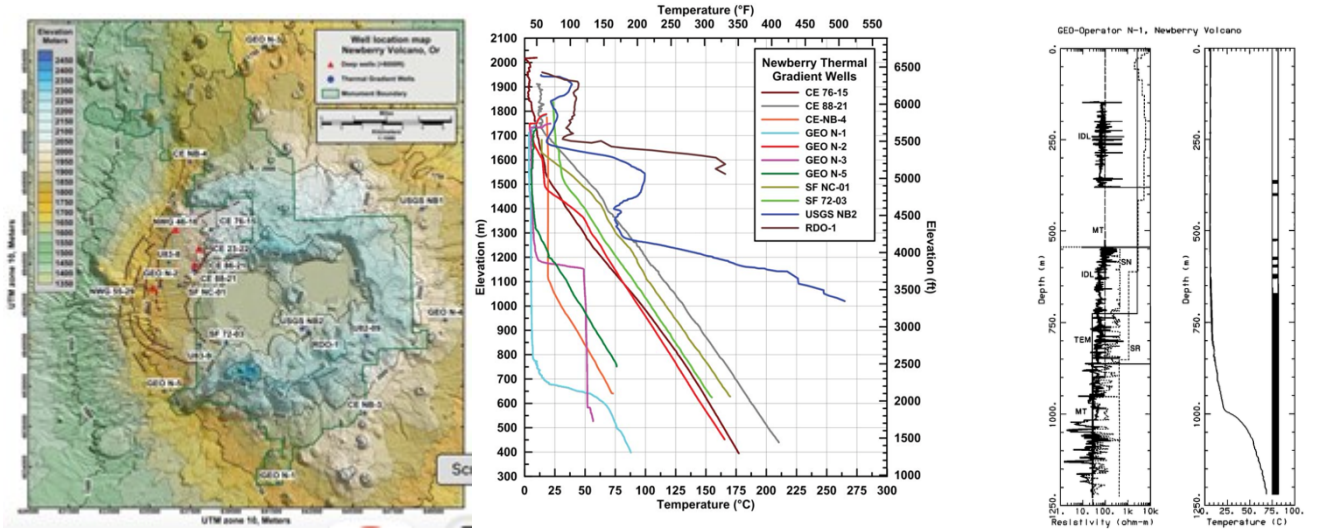

Figure 21. (left) Topographic map of Newberry Volcano with exploration well locations marked. Brown lines are inferred structures from lidar data (from Frone, 2015). (center) Temperature profiles for Newberry Volcano gradient wells (From Frone, 2015). The profile for well GEO N-1 is a light turquoise color. (right) Interpreted layer resistivity-depth functions for legacy 1-D DC Schlumberger array resistivity, transient electromagnetic and MT soundings elsewhere on the volcano for GEO N-1 well (from Fitterman et al., 1988). The deep induction (IDL) and short normal (SN) well logs from GEO N-1 are shown for comparison. Zones of inferred smectite alteration are shown by the black bar on the temperature plot, which is the same temperature profile in the Frone figure reproduced on the left.

As Fitterman, et al (1988) indicates: "Alteration minerals are commonly found in active and fossil hydrothermal systems… While the minerals present are different for each system, commonly found minerals include smectite, illite, mixed layer illite- smectite, zeolite, calcite, chlorite, and epidote; there is usually a correlation between the minerals present and the temperature of the system... Smectite is found at temperatures as high as 200°C. Mixed layer illite-smectite and illite are found at higher temperatures. Zeolites are found at slightly lower temperatures, with the maximum being around 150°C. Calcite is found over a very wide range of temperatures (50°-300°C). Epidote and chlorite are indicative of temperatures in excess of 200°C. The alteration minerals found in test holes Newberry 2 and GEO N-1 are among those commonly found in hydrothermal systems...", and

"The most direct evidence is given by Wright and Nielson [1986], who found that alteration zones in GEO N-1 core which were rich in smectite derived from ash flows had low resistivities (1.5-15 Ωm) on the induction logs." Lévy et al. (2020) notes that the presence of smectite in such systems may indicate recent hydrothermal circulation. They note that "In active hydrothermal systems, the formation of smectite is not only controlled by the geothermal gradient, but also by the convective activity related to recent fault opening and causing boiling as well as chemical disequilibrium… Compared to other clay minerals (e.g. illite, chlorite, kaolinite), smectite is much more conductive… and contributes significantly to the electrical conductivity of rocks, through Electrical Double Layer mechanisms..."

Lévy, et al. (2018) note that "expandable minerals" that form clay caps in geothermal systems are thermodynamically stable from 80°C – 180°C, above which they are replaced progressively by chlorite and other minerals in the event thermodynamic equilibrium conditions exist. They note, however, in active volcanic systems smectite is observed at temperatures higher than 300°C, while in Icelandic volcanic systems discrete chlorite is found only above 270°C.

It is almost certainly the case that hydrothermal alteration products including clays such as smectite are a component of the electrically conductive SRFF feature. The temperature gradient data from nearby well GEO N-1 suggests that this feature is likely the signature of recent, and possibly contemporary hydrothermal circulation. Given that the SRFF extends to at least 3.4 km and possibly to more than 4.5 km below the caldera floor at which point our dataset loses resolving power – depths equivalent to the apparently unconnected but seismically determined melt zone beneath the center of the caldera; that it shallows next to the Big Obsidian Flow, the most recent eruptive feature on the volcano (1,300 ybp); and that it adjoins the Walker Rim crustal fault that provides a likely structural pathway for fluid migration, the south rim/flank feature is posited to be the trace of hydrothermal fluid circulation beneath the south flank as well as hydrothermal mineralization products found in nearby well core samples all possibly fed by deeper sources associated with the adjoining fault zone. The SRFF is not directly connected to the seismic low velocity/melt body beneath the caldera, but rather is the consequence of a separate south flank hydrothermal fluid and melt source at greater depth that is most likely the feeder system for the Big Obsidian Flow.

To establish if our data for the SRFF is consistent with an active hydrothermal system, or even a contemporary melt source, in the next section we report on preliminary modeling of the system to explore the data-driven bounds on porosity, water/brine content and melt content in the SRFF, and in the putative melt zone in the sub-caldera seismic low velocity feature.

3.2 Rhyolite-MELTS Phase Diagram Analysis

We have built thermodynamic models for a multi-component rhyolite-brine, multi-phase system of melt+crystalline, melt, melt+melt volatile product, melt-crystalline-melt volatile product by using Rhyolite-MELTS (Gualda, et al., 2012). We have assumed thermodynamic phase equilibrium for the preliminary results reported here, with the caveat that equilibrium conditions likely do not hold if the SRFF represents a zone of active hydrothermal circulation and mineralization/dissolution/alteration. Nevertheless, even within this limitation we find that by projecting the electrical resistivity, density and seismic v_p values from within our model volume into the resulting phase diagrams, useful inferences can be drawn.

We apply the melt resistivity model of Guo et al (2016), the brine/vapor phase resistivity model of Watanabe et al. (2021) and a modified form of Archie's Law (1942) for a resistivity solid/fluid mixing model. For melt density, we use the DensityX model (Iacovino and Till, 2019), and for the two-phase brine/vapor system we apply the swEoS density model (Span and Wagner, 1996). For the melt-seismic velocity relationship, we use the model of Chu et al. (2010). We have assumed for the resistivity model that the crystalline phase is granite, but this deviates very little from that for rhyolite, whereas for the melt phase we assume rhyolitic melt.

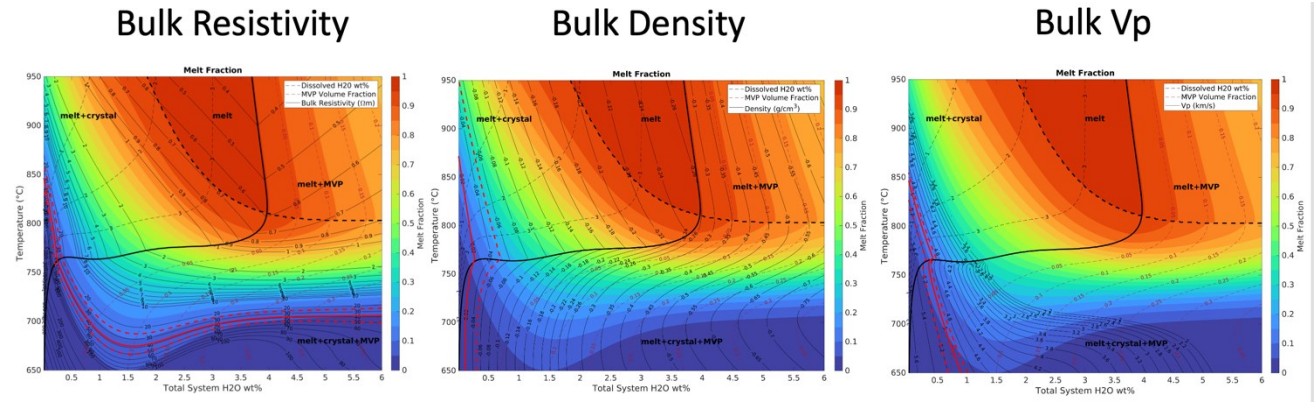

Figure 22. For depths of 4-5 km (110 MPa lithostatic pressure) and temperatures associated with the sub-caldera melt body, in all three plots we show the identical melt fraction vs. temperature and total system H_2O wt% diagrams. Within each plot, the top left quadrant is the zone of H_2O dissolved in the melt (melt + crystal phase); the center top area – entirely melt with H_2O dissolved in the melt; the top right quadrant – melt & pore spaces with liquid or vapor phase H_2O; and on the bottom part of each diagram below the thick line – liquid or vapor phase H_2O in pore spaces totally segregated from melt/crystalline phases.

The solid red lines in Figure 22 conform to the resistivity, density and v_p for the sub-caldera magma body as extracted from the joint MT + gravity model and from the seismic tomography volume. The dashed red lines represent the uncertainty in the models. The independent constraints on temperature and water content from resistivity, density and v_p for the magma body intersect toward the low wt% H_2O end of the phase diagrams. Figure 23 provides a closer-in view of that intersection.

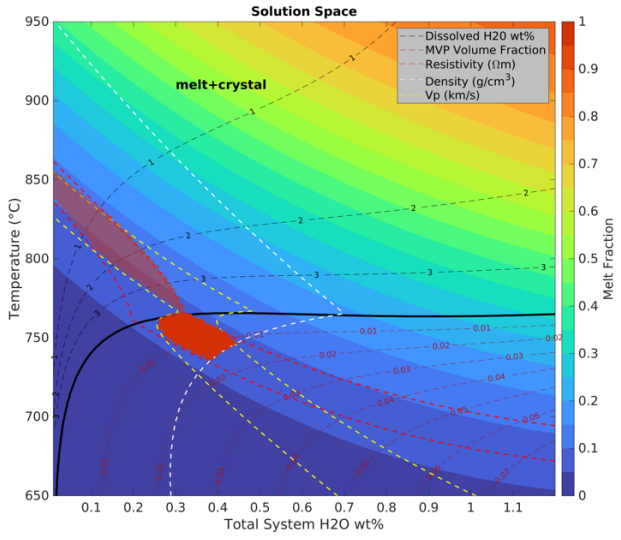

Figure 23. The intersection of resistivity, density and v_p against H_2O fraction showing that all three constraints intersect when there is <0.4 wt% H_2O. The light red zone represents the intersection of the geophysical constraints where melt volatile content is unsaturated, so would tend not to exsolve vapor bubbles whereas the dark red zone is where the same constraints intersect but the melt volatile content is saturated and H_2O vapor phase may exsolve bubbles into the melt.

As shown in Figure 23, for the putative melt body beneath the caldera, the resistivity and density constraints are compatible with the seismic constraints on melt for a rhyolitic system, only if the melt is dry with less that 0.4 wt% H_2O. If the system is completely free of H_2O and up to a limit of about 0.3 wt% H_2O, the melt volatile content will be unsaturated, whereas if the H_2O content is between ~0.3 – 0.4 wt%, it is saturated. Evidence from Heath et al. (2015) of microseisms within the caldera in the depth range used to generate Figure 23 may be evidence for release of saturated melt volatile content in the form of vapor bubbles, but this result is only preliminary, and work is continuing to study this in more detail.

We now consider a similar set of phase relationships, but for conditions within the south caldera rim and flank anomaly (SRFF). This is seen in Figure 24.

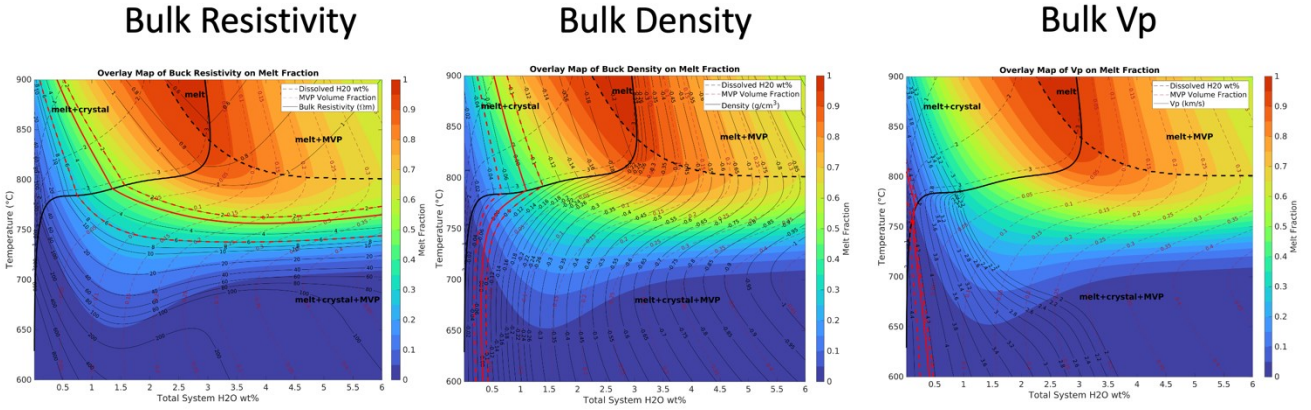

Figure 24. For the volcano's south rim and flank (the SRFF), we assume a depth of 2.5 km and a lithostatic pressure of 62.5 MPa. The same relatively high temperature range is examined here as in Figure 22 to test if the constraints from the resistivity, density and v_p within the SRFF are mutually compatible with any solution allowing for melt. As was the case for Figure 22, The solid red lines conform to the electrical resistivity, density and v_p for the SRFF at this depth. The dashed red lines represent the uncertainty in the model.

In contrast to the phase diagrams for the sub-caldera melt body (Figure 23), within the SRFF (Figure 24) we find that there is no point within this phase space in which the resistivity, melt and v_p constraints intersect. Within the resolving limits of our data, i.e. to depths of ~4.5 km, assuming equilibrium conditions hold, no solution is found for rhyolitic melt content that is consistent with the geophysical model parameters of the SRFF. This doesn't eliminate the possibility that there is a contemporary melt source deeper in the crust beneath or near the southern part of the volcano – the data we've used do not allow us to resolve such a feature.

Given that we don't find evidence for a detectible melt fraction within the SRFF, can our data allow for the existence of brine and constrain its content? This is explored in Figure 25.

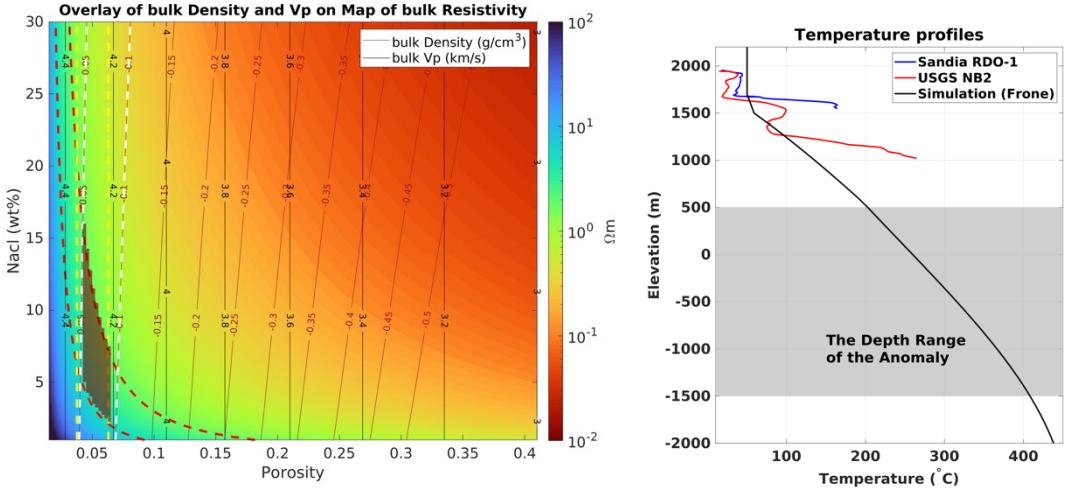

Figure 25. (Right) Frone's (2015) temperature model for Newberry volcano with the depth range of the SRFF in gray. If that model holds for the SRFF, its temperature is bounded between 200°C $\lesssim$ T $\lesssim$ 400°C. (Left) By projecting the modeled bulk density (from the joint MT+gravity inversion) and v_p (from seismic tomograms) onto salinity vs porosity diagram for the resistivity, with the resistivity constraints from the joint MT+gravity inversion appearing as dashed red lines, we find that for this temperature range there is an intersection between the resistivity, density and v_p constraints in salinity-porosity space.

With the significant caveat that equilibrium conditions are assumed, and that Frone's (2015) thermal model for Newberry volcano applies to the volcano's south rim and flank (there are few constraints from temperature wells in the south flank area near the SRFF), we find that the data are consistent with a bulk porosity within the SRFF of ~0.05% and a brine NaCL concentration of ~2-17%.

Both hydrothermal clays (particularly wet smectite) and hot brines within the SRFF are consistent with the density, resistivity and v_p data. In the event that the temperature regime within the SRFF is accurately represented by the Frone model, much of the SRFF is likely to lie beyond the stability limit for clay minerals such as smectite, in which case the conclusion from Figure 25 is that an active, blind hydrothermal system may exist (see previous paragraph). The evidence for advective/convective heat transport in the bottom part of the GEO N-1 well, the warm temperatures there at depth but the suppressed geotherm above as well as the considerable quantity of smectite in the bottom half of GEO N-1 located only ~2 km from the intersection of low density, high conductivity and seismically low v_p sosurfaces in the SRFF would be consist with such a conclusion.

5. CONCLUSION

The Newberry volcano south rim/south flank feature (SRFF) is a zone of low relative density, low seismic velocity and low electrical resistivity that shallows under the south caldera rim end of the Big Obsidian Flow, an area known to be the vent for a sequence of rhyolite eruptions that formed the BOF ~1,300 ybp (Jenson & Chitwood, 2000). The SRFF crosses beneath the south caldera rim and progressively deepens to the south along the volcano's flank. Well GEO N-1 immediately to the west of the SRFF exhibits a depressed geotherm to depth of 1000 m below well head, then below that a sharp, non-linear temperature gradient indicative of a hydrothermal system. The lower half of the well contains considerable smectite. Clay caps in geothermal systems are thermodynamically stable from 80°C – 180°C, above which they are replaced progressively by chlorite and other minerals in the event thermodynamic equilibrium conditions exist. In active volcanic systems smectite is observed at temperatures higher than 300°C, while in Icelandic volcanic systems discrete chlorite is found only above 270°C. Alteration zones in GEO N-1 core were rich in smectite derived from ash flows, with low resistivities (1.5-15 Ωm) on the induction logs – smectite is among the most electrically conductive clays, more so when wet. Smectite and hydrothermal clays such as illite are also seismically slow.

More generally, the relatively low density associated with the south rim/flank anomaly is consistent with elevated porosity and/or/the presence of clays resulting from hydrothermal circulation, and/or the presence of hydrothermal fluids. The temperature gradient data from nearby well GEO N-1 suggests that the anomaly is likely the signature of recent, and possibly contemporary hydrothermal circulation. This is supported by modeling using Rhyolite-MELTS (Gualda, et al, 2012), which indicates that there is no evidence for detectible quantities of melt within the SRFF, but that a bulk porosity within the SRFF of ~0.05% and a brine NaCL concentration of ~2-17% is supported by the geophysical data. If the Frone (2015) thermal model holds for the south rim and south flank of the volcano, since the SRFF extends to depths of at least 3.4 - 4.5 km or more below (but south of) caldera floor depth, it is likely that temperatures higher than the stability field for smectite and most other hydrothermal clays holds, assuming equilibrium conditions. In that event, the geophysical data would be satisfied by the existence of such clays under disequilibrium conditions, which would require active hydrothermal circulation under these conditions, or they would be satisfied by the existence of an active hydrothermal system even in the absence of such clays, chlorites and other mineral products. These depths are also equivalent to the apparently unconnected (but seismically determined) melt zone beneath the center of the caldera. In contrast, the seismically determined melt body beneath the caldera is found to be consistent with the geophysical data given a solution that supports a dry rhyolitic melt with no more than 0.4 wt% H_2O.

In conclusion, by combining a multi-physics data set (MT, gravity, seismic) with joint inversion and interpretation, with geologic mapping, structural interpretation, and well log and core analyses, the south flank of Newberry volcano may present a previously undetected conventional geothermal blind play. This complements the current EGS play on the west flank of Newberry volcano, tapping into a putative pluton/previous volcanic center, that has been extensively studied (and stimulated) in recent decades, and that is under renewed development efforts. Newberry volcano is therefore potentially a multi-site geothermal field, with potential for shared power transmission infrastructure. A logical next step is to drill deep temperature wells within the footprint of the SRFF.

5. ACKNOWLEDGEMENT

The authors acknowledge the funding of this project through US Department of Energy (DOE) Office of Energy Efficiency and Renewable Energy (EERE) Geothermal Technologies Office (GTO) Prime Contract No. DE-AC36-08GO28308, as well as through NREL subcontract SUB-2022-10269 to Enthalpion Energy LLC under the prime contract. This work was authored in part by the National Renewable Energy Laboratory, operated by Alliance for Sustainable Energy, LLC, for the DOE. The views expressed in the article do not necessarily represent the views of the DOE or the U.S. Government. The U.S. Government retains and the publisher, by accepting the article for publication, acknowledges that the U.S. Government retains a nonexclusive, paid-up, irrevocable, worldwide license to publish or reproduce the published form of this work, or allow others to do so, for U.S. Government purposes.

Statement of potential conflict of interest – the first author of this paper is President of Enthalpion Energy LLC, holder of a geothermal lease in the area of the south rim/south flank feature (SRFF). The lease was obtained after Enthalpion Energy LLC concluded its work acquiring MT and gravity data in collaboration with and under the support of NREL in 2022. The field campaign and preliminary modeling was concluded prior to the author becoming aware of a lease auction for that area. The author holds the analysis and interpretation presented here to be based entirely on objective science and not influenced by subjective factors related to the current lease holding.

REFERENCES

Archie, G. The Electrical Resistivity Log as an Aid in Determining Some Reservoir Characteristics: Transactions of the AIME, 146, 54–62, (1942).

Beachly, M.W., et al. Upper crustal structure of Newberry Volcano from P-wave tomography and finite difference waveform modeling. J. Geophys. Res. Solid Earth 117, B10311, (2012).

Bowles-Martinez, E., Schultz, A. Composition of magma and characteristics of the hydrothermal system of Newberry Volcano, Oregon, from magnetotellurics. Geochem. Geophys. Geosyst. 21, e2019GC008831, (2020).

Chu, R., D. V. Helmberger, D. Sun, J. M. Jackson and L. Zhu. Mushy magma beneath Yellowstone, *Geophys. Res. Lett.*, https://doi.org/10.1029/2009GL041656 (2010).

Fitterman, D. V., W. D. Stanley and R. J. Bisdorf (1988). Electrical structure of Newberry Volcano, Oregon, *J. Geophys. Res.*, **93**, No. B9, 10,119-10,134.

Frone, Z. Heat flow, thermal modeling and whole rock geochemistry of Newberry Volcano, Oregon and heat flow modeling of the Appalachian Basin, West Virginia, Ph.D. Dissertation, Southern Methodist University, (2015).

Gualda, G. A. R, M. S. Ghiorso, R. V. Lemons & T. L. Carley. Rhyolite-MELTS: a modified calibration of MELTS optimized for silica-rich, fluid-bearing magmatic systems, *J. Petrology*, **53**, 5, pp 875-890, https://doi.org/10.1093/petrology/egr080, (2012).

Guo, X., L. Zhang, H. Behrens, H., Ni, H. Probing the status of felsic magma reservoirs: Constraints from the P-T-H_2O dependences of electrical conductivity of rhyolitic melt, *Earth and Planet Sci. Lett.,* 433**,** 54-62, (2016).

Heath, B.A., Hooft, E.E.E., Toomey, D.R., Bezada, M.J. Imaging the magmatic system of Newberry Volcano using joint active source and teleseismic tomography. *Geochem. Geophys. Geosyst.* **16**, 4433–4448, (2015).

Iacovino, K and C. B. Till. DensityX: A program for calculating the densities of magmatic liquids up to 1,627 ^{o}C and 30 kbar, *Volcanica*, **2**, No 1 (2019).

Jenson, R. A. and L. A. Chitwood. Geologic overview of Newberry Volcano, in *Friends of the Pleistocene – Pacific Northwest Cell – 2000*, pp 28 – 31, (2000).

Lévy, B. Gilbertt, F. Sigmundsson, Ø. G. Fløvenz, G. P. Hersir, P. Briole, P. A. Pezard. The role of smectites in the electric conductivity of active hydrothermal systems: electrical properties of core samples from Krafla volcano, Iceland, *Geophys. J. Intl.*, **215**, 3, 1558-1582, https://doi.org/10.1093/gji/ggy342, (2018).

Lévy, L., T. Fridriksson, N. Findling, B. Lanson, B. Fraisse, N. Marino and B. Gilbert. Smectite quantification in hydrothermally altered volcanic rocks, *Geothermics*, **85**, https://doi.org/10.1016/j.geothermics.2019.101748, (2020).

MacLeod, N.S., Sherrod, D.R., Chitwood, L.A., and Jensen, R.A. Geologic map of Newberry Volcano, Deschutes, Klamath, and Lake Counties, Oregon: U.S. Geological Survey Miscellaneous Investigations Series Map I–2455, 2 sheets, scale 1:62,500, pamphlet, 23 p, (1995).

Mark-Moser, M., Schultz, J., Schultz, A., Heath, B., Rose, K., Urquhart, S., Bowles-Martinez, E., Vincent, P. A conceptual geologic model for the Newberry Volcano EGS site in central Oregon: constraining heat capacity and permeability through interpretation of multicomponent geosystems data. In: PROCEEDINGS, 41st Workshop on Geothermal Reservoir Engineering. Stanford University, Stanford, California, (2016).

Pauling, H., A. Schultz, E. Bowles-Martinez, X. Tu, C. Hopp. A. Bonneville and A, Kolker. Exploring for superhot geothermal targets in magmatic settings: 2022 field campaign at Newberry Volcano, PROCEEDINGS, 48th Workshop on Geothermal Reservoir Engineering, Stanford University, Stanford, California, February 6-8, 2023, SGP-TR-224, (2023).

Span R and Wagner W. A new equation of state for carbon dioxide covering the fluid region from the triple-point temperature to 1100 K at pressures up to 800 MPa. J Phys Chem Ref Data 25(6): 1509–96, (1996).

Tu, X., Zhdanov, M.S. Joint focusing inversion of marine controlled-source electromagnetic and full tensor gravity gradiometry data. Geophysics 87, K35–K47, (2022).

Watanabe, N., Y. Yamaya, K. Kitamura and T. Mogi. Viscosity-dependent empirical formula for electrical conductivity of H_2O fluids at elevated temperatures and high salinity, *Fluid Phase Equilibria*, **541**, 113187, (2021).